ORIGINAL ARTICLE

Multi-core–shell-structured LiFePO$_4$@Na$_3$V$_2$(PO$_4$)$_3$@C composite for enhanced low-temperature performance of lithium-ion batteries

Xing-Xing Gu* , **Shuang Qiao, Xiao-Lei Ren, Xing-Yan Liu, You-Zhou He, Xiao-Teng Liu, Tie-Feng Liu***

Abstract In this work, a multi-core–shell-structured LiFePO$_4$@Na$_3$V$_2$(PO$_4$)$_3$@C (LFP@NVP@C) composite was successfully designed and prepared to address inferior low-temperature performance of LiFePO$_4$ cathode for lithium-ion batteries. Transmission electron microscopy (TEM) confirms the inner NVP and outer carbon layers co-existed on the surface of LFP particle. When evaluated at low-temperature operation, LFP@NVP@C composite exhibits an evidently enhanced electrochemical performance in term of higher capacity and lower polarization, compared with LFP@C. Even at − 10 °C with 0.5C, LFP@NVP@C delivers a discharge capacity of ca. 96.9 mAh·g^{-1} and discharge voltage of ca. 3.3 V, which is attributed to the beneficial contribution of NVP coating. NASICON-structured NVP with an open framework for readily insertion/desertion of Li$^+$ will effectively reduce the polarization for the electrochemical reactions of the designed LFP@NVP@C composite.

Keywords LiFePO$_4$@Na$_3$V$_2$(PO$_4$)$_3$@C composite; Multi-core–shell; Low-temperature; Lithium-ion batteries

1 Introduction

LiFePO$_4$ (LFP) has been receiving much attention as alternative cathode material for lithium-ion batteries (LIBs) due to its excellent thermal safety, environmental friendliness, and abundant sources for low cost [1–3]. Although LFP suffers from intrinsically low electronic and ionic conduction, intensively studies and modifications during recent two decades have enabled a satisfactory rate capability at ambient and high temperatures by methods of coating conductive agents, doping alien ions, and tailoring morphology [4–10]. However, in cold climates and high-altitude drones, LIBs are required to work at subzero temperature. Cold temperature causes sluggish diffusion rate and slow reaction kinetics. Therefore, both discharge capacity and output voltage of LFP are substantially dropped [11–13].

Previous researches have shown that inferior low-temperature performance of LFP is attributed to low Li$^+$ diffusion of electrode materials and high charge-transfer resistance of electrolyte/electrode interface [13, 14]. Most of the approaches to solve this issue are optimizing electrolyte by introducing additives to tune electrolyte/electrode interface for reducing charge-transfer resistance [11, 12, 15–17]. In contrast with the electrolyte development, insufficient strides have been achieved in electrode materials design for the low-temperature application. Generally, increasing insertion/desertion channels could accelerate the charge/discharge

X.-X. Gu*, X.-L. Ren, X.-Y. Liu, Y.-Z. He
Chongqing Key Laboratory of Catalysis and New Environmental Materials, College of Environment and Resources, Chongqing Technology and Business University, Chongqing 400067, China
e-mail: x.gu@ctbu.edu.cn; xingxing.gu@northumbria.ac.uk

X.-X. Gu, X.-T. Liu
Faculty of Engineering and Environment, Northumbria University, Newcastle upon Tyne NE1 8ST, UK

S. Qiao
GRINM Group Co., Ltd., Beijing 100088, China

T.-F. Liu*
College of Materials Science and Engineering, Zhejiang University of Technology, Hangzhou 310014, China
e-mail: tiefengliu@zjut.edu.cn

procedure, even at low-temperature surrounding. Previously, the low-temperature performance of LFP was effectively enhanced by coating Li$_3$V$_2$(PO$_4$)$_3$ material that offers three-dimensional (3D) diffusion channels for insertion/desertion of Li$^+$, in contrast to one-dimensional (1D) diffusion channels of Li$^+$ for olivine-structured LFP along the b-axis [18, 19]. Recently, our group has demonstrated the analogous advantages for providing 3D fast Na$^+$ diffusion channels in NASICON-structured Na$_3$V$_2$(PO$_4$)$_3$ (NVP) crystals, as thus, which is used as an excellent cathode material for all-climate sodium ion batteries systems [19, 20]. Considering the ionic radius of Li$^+$ is much smaller than that of Na$^+$ (0.076 nm vs. 0.102 nm) [21, 22], it can be expected that Li$^+$ could also transfer rapidly in the ion-diffusion channels of NVP. Therefore, coating NVP layer as a fast Li$^+$ diffusion intermediary should be an effective strategy to assistant the insertion/desertion of Li$^+$ for LFP at low temperature.

In this work, a multi-core–shell-structured LFP@NVP@C composite was designed, in which LFP particles are the cores, NVP as the inner layer to improve the interface kinetics and carbon layer as the outer layer to enhance electronic conductivity of the whole composite, as illustrated in Fig. 1. The low-temperature performances of as-prepared electrodes were systematically investigated through electrochemical characterizations. At − 10 °C with the rate of 0.5C, LFP@NVP@C delivered a discharge capacity of 96.9 mAh·g^{-1}, which is higher than LFP@C (80.2 mAh·g^{-1}) without the NVP inner layer and mixed LFP@C/NVP@C composite (80.6 mAh·g^{-1}). This enhancement is due to the NVP layer with 3D diffusion channels on the surface of LFP, enabling more insertion/desertion of Li$^+$ into the crystals and reducing charge-transfer resistance at low temperatures. We do believe this work will open an important window for the research of multifunctional materials for application in low-temperature battery systems.

2 Experimental

2.1 Material synthesis

LFP@C and NVP@C composites were synthesized, respectively, according to our previous report [10, 20].
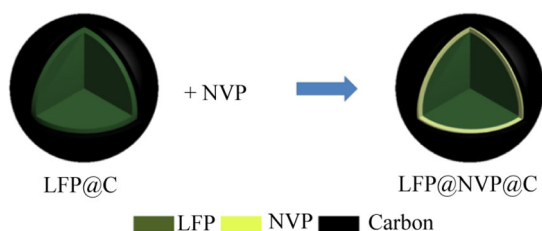

Fig. 1 Schematic illustration used to synthesize LFP@NVP@C composite

LFP@C was prepared after experiencing the process of rheological phase, high-energy ball milling and a subsequent carbothermal reduction. While NVP@C was prepared through solid-state strategy, combined with two-step ball-milling and a subsequent carbothermal reduction. In order to synthesize LFP@NVP@C composite, mixture of LFP@C powder and the precursor of NVP@C (95:5 by weight) was ball milled at 300 r·min^{-1} for 3 h and then calcined at 700 °C for 8 h under Ar atmosphere. For comparison, LFP@C/NVP@C powder was obtained by mixing LFP@C and NVP@C composites (95:5 by weight).

2.2 Materials characterizations

The materials phases investigated by X-ray diffractometer (XRD, Rigaku MiniFlex 600, Japan) was used to analyze the materials phases, the diffraction angle was scanned from 10° to 60° using the Cu Kα radiation (λ = 0.154178 nm). The high-resolution transmission electron microscopy (HRTEM, F30) was used to investigate the morphology and microstructure of as-prepared samples. The elemental compositions of the prepared samples were examined by inductively coupled plasma atomic emission spectrometry (ICP-AES, Perkin Elmer, 300DV) and X-ray photoelectron spectrometer (XPS, Axis Ultra, Kratos Analytical Ltd.).

2.3 Electrochemical measurements

The electrodes slurry was prepared by mixing the as-prepared samples with carbon black and PVDF (polyvinylidene fluoride) binder in a certain weight ratio of 80:10:10, and N-methylpyrrolidone (NMP) was the slurry solvent. After pasting on the Al foil and drying overnight in vacuum at 100 °C, the working electrode could obtain by using the mold (14 mm in diameter) to cut. The cathode loading was about 2–3 mg·cm^{-2}. The CR2025 coin cells were assemble in Ar-filled glove box, which Li foil served as the counter electrode, LiPF$_6$ in carbonate as electrolyte and Celgard 2400 as separator. The LAND CT-2001A (Wuhan, China) battery testing system was used to investigate the galvanostatic charge–discharge behaviors. Cyclic voltammetry (CV) measurements were performed on CHI 660E electrochemical workstation (CHI Instrument, Shanghai, China). The testing voltage window range was 2.5–4.2 V.

3 Results and discussion

Generally, LFP is modified with carbon layer for core–shell structure to enhance electronic conductivity of the composite [6, 8, 23, 24]. Here, we intend to further modify the surface of LFP with NVP inner layer for enhancing

insertion/desertion of Li^+ through constructing multi-core–shell structure. Microstructure of LFP@C and LFP@NVP@C samples were characterized by TEM in Fig. 2. The LFP@C composite is composed of LFP with a high crystallinity and amorphous carbon coating of 2–3 nm (Fig. 2a). Although core–shell-structured LFP@C composite allows a sufficient diffusion of Li^+ in the crystals and electron transfer via outer carbon layer, 1D diffusion channels of LFP along the *b*-axis only offer a limited window for insertion/desertion of Li^+. The LFP@NVP@C displayed dual coatings consisted of NVP inner layer and carbon outer layer (Fig. 2b). It can be observed the interplanar spacing of 0.30 nm corresponds to (121) face of LFP and interplanar spacing of 0.31 nm corresponds to (031) face of NVP, respectively [10, 20]. In addition, there are evident boundaries between LFP, NVP and carbon. The thicknesses of NVP and carbon layers are 3–4 nm and 1–2 nm, respectively. High-angle annular dark-field scanning TEM (HAADF-STEM) images characterized elemental distribution of Fe, V and Na in LFP@NVP@C, as shown in Fig. 2c–f. Uniform distributions of elemental V and Na in the periphery of elemental Fe were witnessed, indicating the existence of a thin NVP coating layer. Owing to 3D Li^+ diffusion channels of NASICON, the NASICON-structured NVP is supposed to be an ionic-conductive intermediary with a highly open framework to introduce Li^+ into the composite.

Figure 3 shows XRD patterns of LFP@NVP@C and LFP@C. It can be observed that all characteristic peaks of LFP@NVP@C and LFP@C are indexed as ordered orthorhombic olivine LFP phase (JCPDS No. 81-1173), illustrating that low amount of addition of NVP won't influence LFP crystal structure. No traces of carbon in LFP@NVP@C and LFP@C were detected due to that residual carbon is amorphous [10]. The carbon contents of LFP@NVP@C and LFP@C are 1.85 wt% and 1.35 wt%, respectively. No diffraction peaks of LFP@NVP@C corresponding to NVP phase were collected due to low amount of NVP component. ICP was further employed to characterize the elemental compositions of LFP@NVP@C and demonstrated that the content of V element was ca. 1.08 wt%, which is consistent well with the V weight ratio of raw materials (1.11 wt%). Further structure information about LFP@NVP@C was characterized by XPS, as shown in Fig. 4. V was confirmed in LFP@NVP@C. High resolution spectrum of C 1s of LFP@NVP@C shows that there is most of sp^2-type carbon, indicating a highly graphitized carbon layer that can facilitate electronic migration [25]. In the high resolution XPS spectrum of V 1s, the peak at binding energy of 515.75 eV belongs to the V(III) [20].

The galvanostatic charge/discharge tests at various temperatures of LFP@NVP@C and LFP@C (shown in Fig. 5) were first investigated. At a rate of 0.5C, LFP@NVP@C electrode shows reversible capacities of
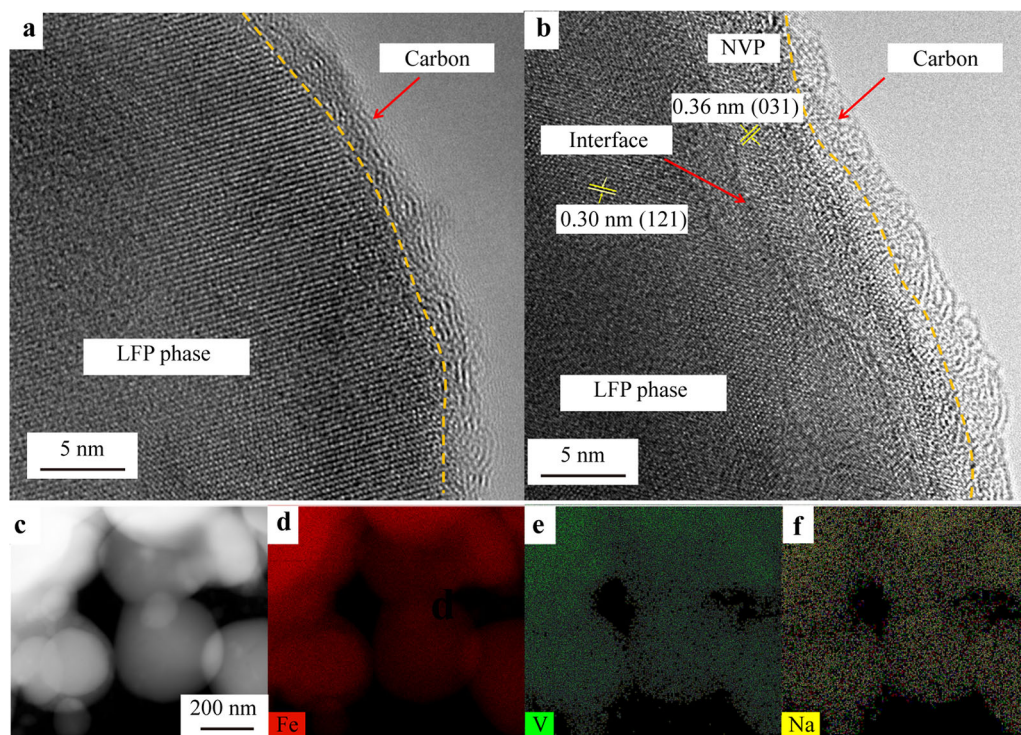

Fig. 2 TEM images of **a** LFP@C and **b** LFP@NVP@C; HAADF-STEM image for LFP@NVP@C: **c** position and elemental distribution of **d** Fe, **e** V and **f** Na

160.9, 111.8, 96.9 and 81.3 mAh·g^{-1} at 23, 0, − 10 and − 25 °C, respectively, which are 2.2%, 3.6%, 15.5% and 18.6% higher than that of LFP@C. Compared with LFP@C, LFP@NVP@C delivers lower charge plateaus as well as higher discharge plateaus, indicating a smaller polarization for interfacial reaction between electrolyte and electrode. Even at − 25 °C, LFP@NVP@C delivers discharge voltage of ca. 3.2 V, respectively, which potentially ensures sufficient power density of LIBs at low temperatures. Coulombic efficiencies of LFP@NVP@C are near 100% at various temperatures. Therefore, LFP@NVP@C exhibits a better electrochemical performance than LFP@C due to the contribution of NVP layer. The NASICON-structured NVP has open framework to offer fast insertion/desertion of Li$^+$ for LFP@NVP@C.

Rate performances of as-prepared electrodes containing LFP@C/NVP@C were further evaluated at various temperatures, as shown in Fig. 6. At 23 °C, LFP@NVP@C,
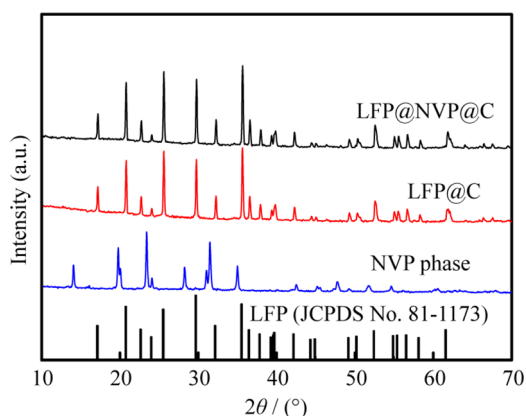

Fig. 3 XRD patterns of LFP@NVP@C, LFP@C, NVP [18], and LFP (JCPDS No. 81–1173)
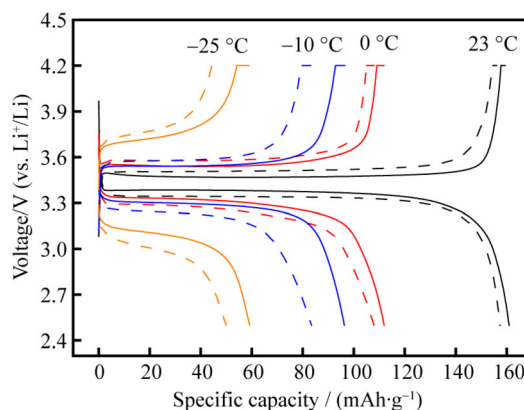

Fig. 5 Electrochemical results of LFP@NVP@C (solid line) and LFP@C (dash line) at various temperatures with 0.5C
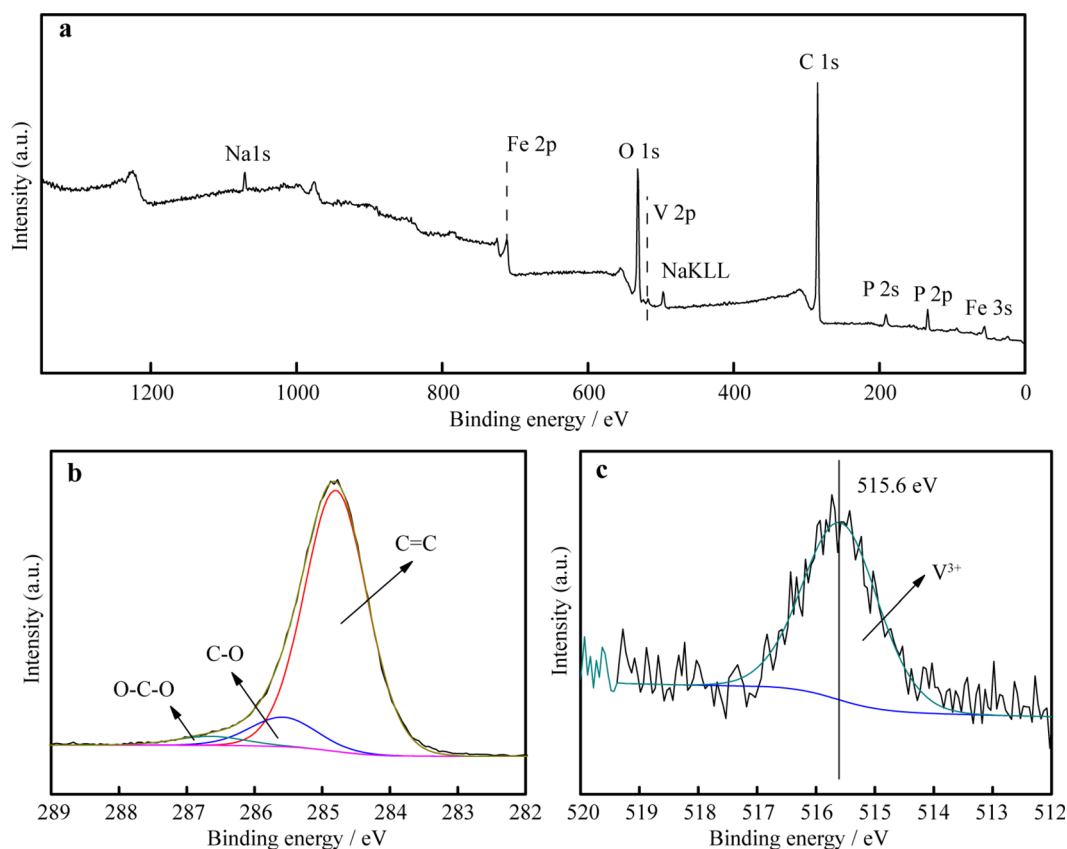

Fig. 4 XPS of LFP@NVP@C: **a** XPS survey, **b** high resolution of C 1s curve, and **c** high resolution of V 2p curve

LFP@C, and LFP@C/NVP@C electrodes exhibit similar electrochemical performances at most rates. Room temperature ensures enough reaction kinetics for the release of capacity of electrode materials. Only one difference for three as-prepared electrodes occurs at the rate of 10.0C. LFP@NVP@C and LFP@C/NVP@C deliver discharge capacities of ca. 100.1 and 93.0 mAh·g^{-1}, respectively, which both exceed LFP@C (82.3 mAh·g^{-1}), indicating that the addition of NVP into LFP is effective for rate performance. In addition, the discharge capacity of LFP@NVP@C is higher than that of LFP@C/NVP@C, illustrating that NVP layer based on multi-core–shell structure plays a beneficial role on facilitating more insertion/desertion of Li$^+$ into LFP crystal. As temperature decreased, effectiveness of NVP coating on improvement of low-temperature performance becomes more distinct. In contrast to LFP@C suffering from inferior low-temperature performance, LFP@NVP@C exhibits enhanced electrochemical properties of Li$^+$ storage. At 0 °C, discharge capacities of LFP@NVP@C are 111.8, 97.6, 84.4 and 61.8 mAh·g^{-1} at 0.5C, 1.0C, 2.0C and 5.0 C, respectively, which are 8.3%, 10.4%, 16.1% and 33.7% higher than that

of LFP@C. Interestingly, discharge capacities of LFP@C/NVP@C are side by side with that of LFP@C at less than 5.0C, while are much close to that of LFP@NVP@C at 10.0C. The NVP@C has been reported to have an excellent low-temperature performance, and therefore NVP@C makes major contribution for discharge capacity of mixed LFP@C/NVP@C electrode [13, 20]. At − 10 °C, LFP@NVP@C still delivered discharge capacities of 96.9, 82.2, 66.7 and 41.6 mAh·g^{-1} at 0.5C, 1.0C, 2.0C and 5.0C, respectively. Even at − 25 °C, LFP@NVP@C exhibited the best rate performance among three as-prepared electrodes. The above results have proved that the NVP with 3D framework and multi-core–shell structure could significantly enhance the performance of LFP@NVP@C at low-temperature. Moreover, the rate performances of LFP@NVP@C below − 20 °C is compared with that reported in previous work, as shown in Table S1.

In order to understand the mechanisms of LFP@NVP@C with enhanced low-temperature performances, the electrochemical kinetics of LFP@NVP@C and LFP@C were compared by investigating the CV curves as shown in Fig. 7. A pair of redox peaks of
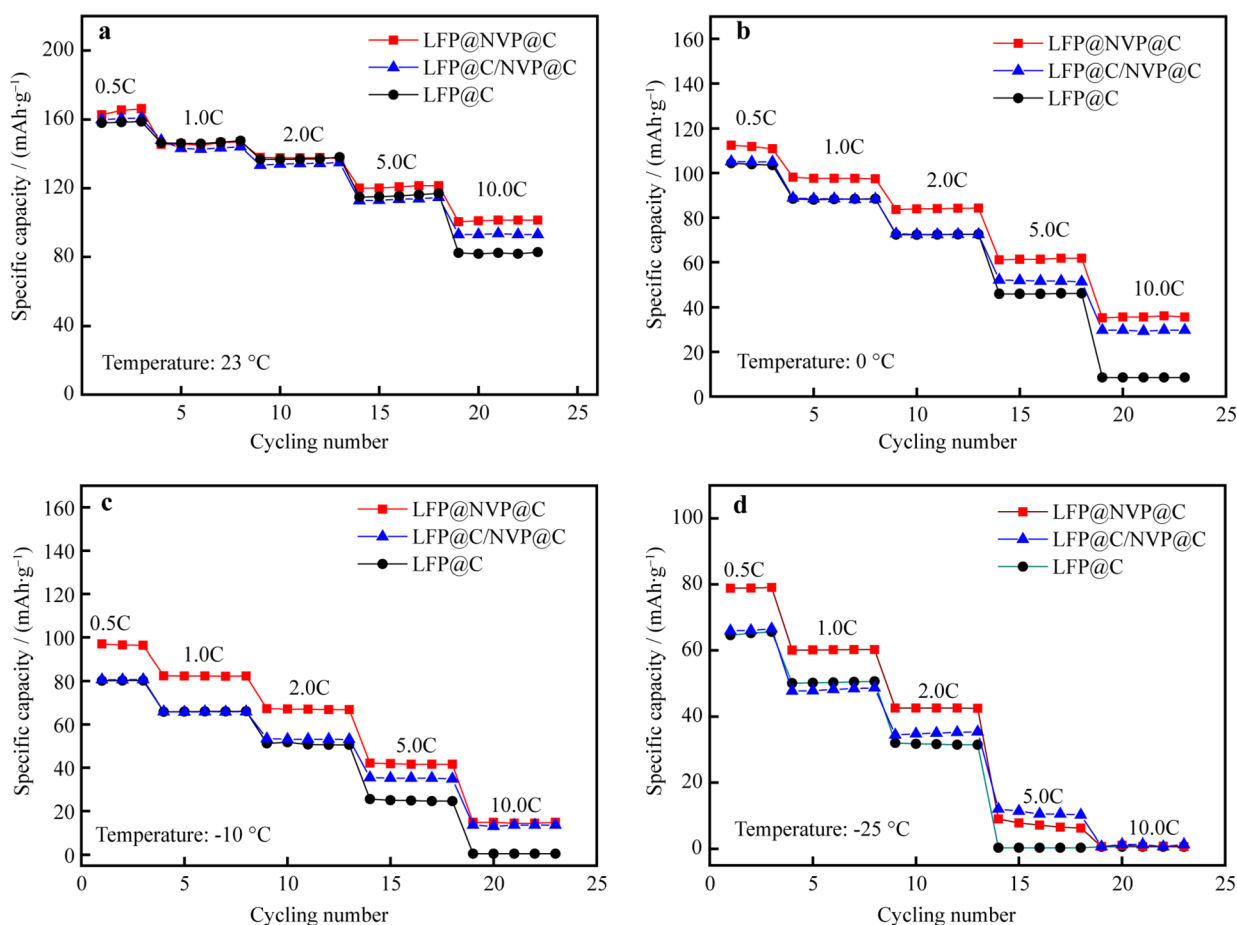

Fig. 6 Rate performance of LFP@NVP@C, LFP@C and LFP@C/NVP@C at different temperatures: **a** 23 °C; **b** 0 °C; **c** − 10 °C; **d** − 25 °C

LFP@C were evidently collected at 23 °C, corresponding to Li$^+$ insertion/de-insertion in LFP crystals that are in conjunction with Fe^{2+}/Fe^{3+} redox couple [6, 10, 26]. As operating temperature decreases down to − 25 °C, the potential interval between anodic/cathodic peaks increases from 333 to 787 mV and peak current drops to a quarter of value at room temperature, which indicates a slowdown of electrochemical reactions of LFP@C. As for LFP@NVP@C, similar to LFP@C, increased polarization and reduced peak current were also observed with operating temperature decreasing. Potential intervals of LFP@NVP@C are 298, 442, 579 and 758 mV at 25, 0, − 10 and − 25 °C, respectively. All the values are lower than that of LFP@C, implying NVP coating layer could relieve the polarization of the LFP@NVP@C electrode.

Then the electrochemical impendence spectra (EIS) at various temperatures were analyzed. As displayed in Fig. 8a, b, as operating temperature decreases, the diameters of semicircles in the profiles of LFP@C//Li and LFP@NVP@C//Li half-cell become significantly larger, respectively. Similarly, the EIS curves of symmetric Li//Li cell also demonstrate a rapidly increased semicircle diameter and thus increased impedance (Fig. 8c). Such increases are well consistent with our recent previous works that charge-transfer resistances of half-cell increasing at low temperatures are mainly attributed to the metallic anode [19, 20, 27], which has demonstrated that using half-cell was not best mode to assess charge-transfer resistance of targeted materials.

Therefore, the EIS spectra of LFP@C and LFP@NVP@C with symmetric cells were further assessed. As shown in Fig. 9a, b, symmetric LFP@C//LFP@C and LFP@NVP@C//LFP@NVP@C cells offer a single semicircle with similar diameters, illustrating that the Li electrode is responsible for the increased impedance [20]. In EIS curves of Fig. 9a, b, the intersection on the x-axis represents bulk resistance of the cell (R_u) including the
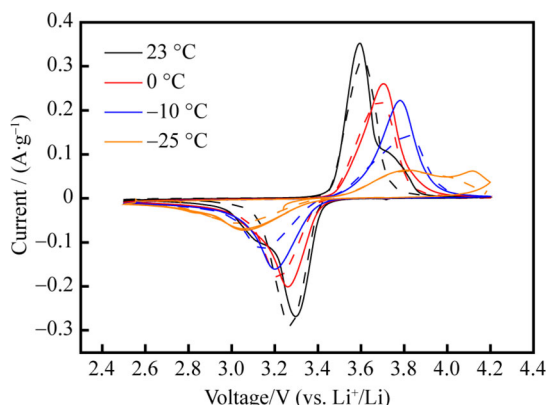
electrolyte and electrodes [4], and semicircle diameter represents corresponding charge-transfer resistance (R_{ct}) reflecting electrochemical kinetics of interfacial reaction [19]. All the values of R_u and R_{ct} are listed in Table 1. The R_u values gradually increase with temperature decreasing can be attributed to slow down Li$^+$ diffusion in the electrolyte [28–32]. An increase in the values of R_{ct} indicates that decreased operating temperatures make reaction kinetics of electrode difficult. Compared with LFP@C, LFP@NVP@C exhibits lower R_{ct} values from 43.74 to 54.55 Ω with temperature decreasing. The NVP offers easy access to Li$^+$ for LFP and thus enables LFP@NVP@C more capacity and lower polarizations than LFP@C during the charge/discharge. In addition, the apparent Li$^+$ diffusion coefficient (D_{Li}) is calculated by the straight slope lines at low frequency region [31, 33, 34]. The Warburg coefficient (σ) can be calculated by Eq. (1):

$$|Z'| = R_s + R_{ct} + \sigma\omega^{-0.5} \tag{1}$$

where the Y-axis of $-Z_{re}'$ represents imaginary part of impedance (Z'), while the X-axis of Z_{im}' represents real part of impedance (Z'), ω is frequency, and σ is Warburg coefficient. The plot of Z_{im} versus the reciprocal square root of the low angular frequency is given in Fig. 9c, d. The slope of the fitted line is the Warburg coefficient (σ). The calculated values of σ for LFP@NVP@C and LFP@C are given in Table 1. Subsequently, because ionic diffusion coefficient (D_{Li}, cm^2·s^{-1}) is inversely proportional to σ, the D_{Li} values can be further calculated by the following Eq. (2):

$$D_{Li} = R^2T^2/2A^2n^4F^4c^2\sigma^2 \tag{2}$$

where R is the gas constant, T is the absolute temperature (K), A is the apparent area of electrode (cm^2), n is the number of electrons per molecule during the intercalation (n = 1), F is the Faraday constant, c is the Li$^+$ concentration (mol·cm^{-3}) and σ is the Warburg coefficient. Therefore, the calculated D_{Li} values at various temperatures are shown in Table 1.

The variation of the values of D_{Li} is higher for LFP@C than LFP@NVP@C, which is benefited from NVP layer with a stable 3D framework offering sufficient interstitial window to allow fast insertion/desertion of Li$^+$ into the crystal [35]. The reduced charge-transfer resistance and improved insertion/desertion of Li$^+$ bring an enhanced low-temperature performance of LFP@NVP@C.

4 Conclusion

A multi-core–shell-structured LFP@NVP@C composite was successfully synthesized to enhance low-temperature performance of LIBs. NVP demonstrates an open
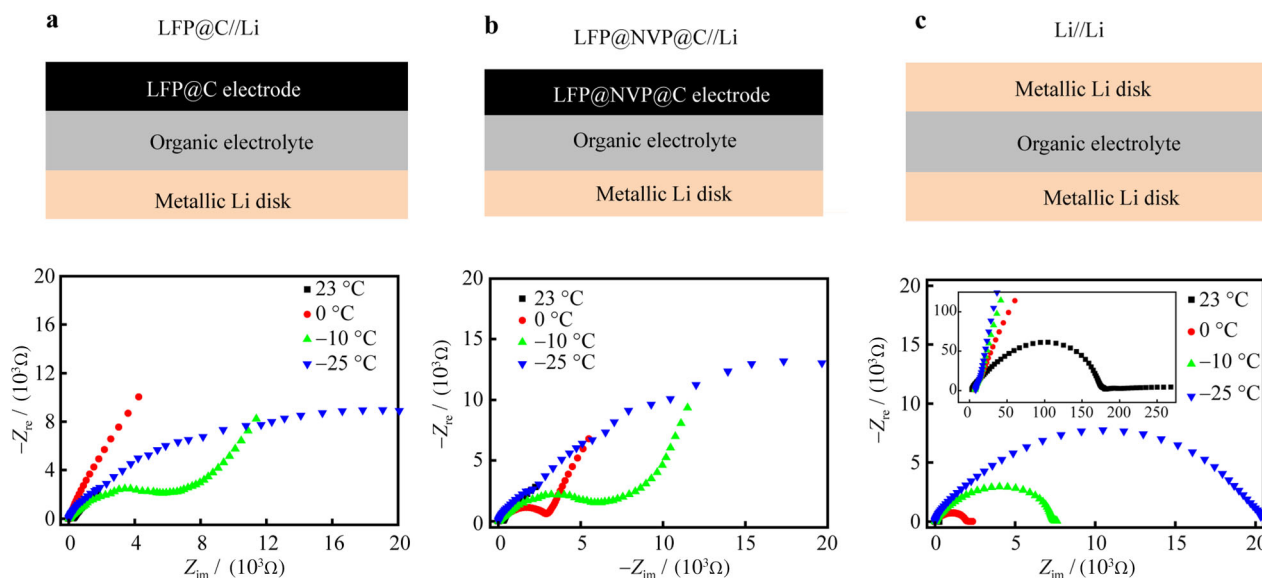

Fig. 7 CV curves of LFP@NVP@C (solid line) and LFP@C (dash line) electrode with scanning rate of 0.1 mV·s^{-1}

Fig. 8 EIS characterizations at different temperatures: cell structure and resultant EIS curves of **a** LFP@C, **b** LFP@NVP@C, and **c** symmetric Li disks
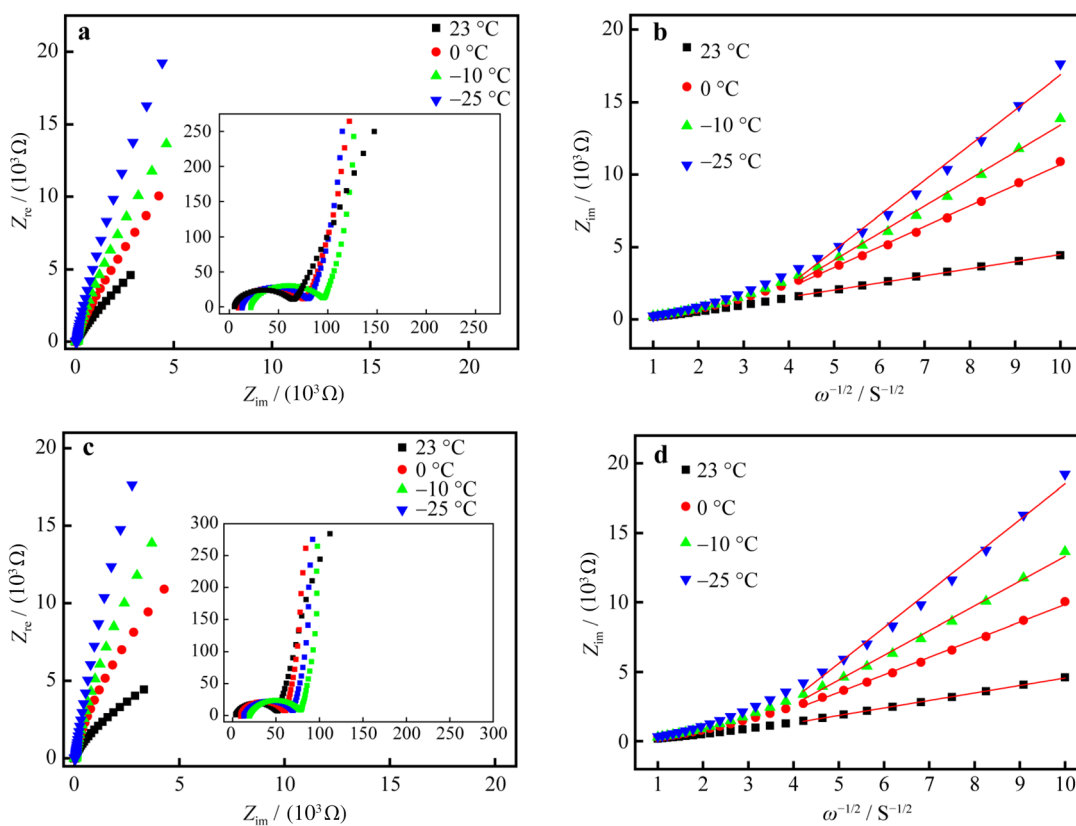

Fig. 9 EIS characterizations of symmetrical electrode at different temperatures: EIS curves of **a** LFP@NVP@C and **b** LFP@C; fitting curves of $-Z_{im}$ and $\omega^{-1/2}$ at low frequency region for **c** LFP@NVP@C and **d** LFP@C

framework for easy insertion/desertion of Li$^+$ into/out of the crystal, and the introduction of NVP interlayer is to modify the surface of LFP crystal by offering more diffusion channels of Li$^+$. As the temperature falls,

LFP@NVP@C exhibited an enhanced low-temperature performance by ca. 8%–33% in comparison with LFP@C, which is attributed to reduced charge-transfer resistance and enhanced Li$^+$ diffusion. Even at -10 °C with 0.5 C,

Table 1 R_u, R_{ct}, σ and D_{Li} values of LFP@C and LFP@NVP@C

Parameters	LFP@C				LFP@NVP@C			
	23 °C	0 °C	− 10 °C	− 25 °C	23 °C	0 °C	− 10 °C	− 25 °C
R_u/Ω	3.89	8.89	16.76	26.57	3.69	9.36	13.09	19.41
R_{ct}/Ω	51.41	70.08	78.36	79.32	43.74	48.32	52.18	54.55
σ/Ω	507.81	1556.53	2060.50	2689.49	490.69	1416.80	1863.61	2421.32
D_{Li}/(10^{-18} cm$^2\cdot$s^{-1})	110	9.96	5.28	2.75	117	12.02	6.449	3.40

LFP@NVP@C delivered a discharge capacity of ca. 96.9 mAh·g^{-1} and discharge voltage of ca. 3.3 V. Our results suggest that tuning the surface of cathodes or anodes with materials of multi-dimensional diffusion channels is an effective method to enhance low-temperature performance of LIBs.

References

[1] Dimesso L, Forster C, Jaegermann W, Khanderi JP, Tempel H, Popp A, Engstler J, Schneider JJ, Sarapulova A, Mikhailova D, Schmitt LA, Oswald S, Ehrenberg H. Developments in nanostructured LiMPO$_4$ (M = Fe Co, Ni, Mn) composites based on three dimensional carbon architecture. Chem Soc Rev. 2012; 41(15):5068.

[2] Li X, Jiang YZ, Li XK, Jiang HX, Liu JL, Feng J. Electrochemical property of LiFePO$_4$/C composite cathode with different carbon sources. Rare Met. 2018;37(9):743.

[3] Zhou JX, Shen XQ, Jing MX, Zhan Y. Synthesis and electrochemical performances of spherical LiFePO$_4$ cathode materials for Li-ion batteries. Rare Met. 2006;25(1):19.

[4] Wang B, Abdulla W, Wang D, Zhao XS. A three-dimensional porous LiFePO$_4$ cathode material modified with a nitrogen-doped graphene aerogel for high-power lithium ion batteries. Energy Environ Sci. 2015;8(3):869.

[5] Wang B, Liu T, Liu A, Liu GJ, Wang L, Gao TT, Wang DL, Zhao XS. A hierarchical porous C@LiFePO$_4$/carbon nanotubes microsphere composite for high-rate lithium-ion batteries: combined experimental and theoretical study. Adv Energy Mater. 2016;6:1600426.

[6] Liu TF, Zhang YP, Chen C, Lin Z, Zhang SQ, Lu J. Sustainability-inspired cell design for a fully recyclable sodium ion battery. Nat Commun. 2019;10:1.

[7] Wang X, Feng Z, Hou X, Liu L, He M, He X, Huang JT, Wen Z. Fluorine doped carbon coating of LiFePO$_4$ as a cathode material for lithium-ion batteries. Chem Eng J. 2020;379:122371.

[8] Zhang Y, Xin P, Yao Q. Electrochemical performance of LiFePO$_4$/C synthesized by sol–gel method as cathode for aqueous lithium ion batteries. J Alloys Compd. 2018;741:404.

[9] Busson C, Blin MA, Guichard P, Soudan P, Crosnier O, Guyomard D, Lestriez B. A primed current collector for high performance carbon-coated LiFePO$_4$ electrodes with no carbon additive. J Power Sources. 2018;406:7.

[10] Liu T, Zhao L, Wang D, Zhu J, Wang B, Guo C. Carbon-coated single-crystalline LiFePO$_4$ nanocomposites for high-power Li-ion batteries: the impact of minimization of the precursor particle size. RSC Adv. 2014;4(20):10067.

[11] Liao XZ, Ma ZF, Gong Q, He YS, Pei L, Zeng LJ. Low-temperature performance of LiFePO$_4$/C cathode in a quaternary carbonate-based electrolyte. Electrochem Commun. 2008;10: 691.

[12] Chen K, Yin S, Xue D. Active La–Nb–O compounds for fast lithium-ion energy storage. Tungsten. 2019;1:287.

[13] Liao L, Zuo P, Ma Y, Chen X, An Y, Gao Y, Yin G. Effects of temperature on charge/discharge behaviors of LiFePO$_4$ cathode for Li-ion batteries. Electrochim Acta. 2012;60(15):269.

[14] Li C, Hua N, Wang C, Kang X, Tuerdi W, Han Y. Effect of Mn^{2+}-doping in LiFePO$_4$ and the low temperature electrochemical performances. J Alloys Compd. 2011;509:1897.

[15] Liao L, Cheng X, Ma Y, Zuo P, Fang W, Yin G, Gao Y. Fluoroethylene carbonate as electrolyte additive to improve low temperature performance of LiFePO$_4$ electrode. Electrochim Acta. 2013;87:466.

[16] Xu CC, Wang Y, Li L, Wang YJ, Jiao LF, Yuan HT. Hydrothermal synthesis mechanism and electrochemical performance of LiMn$_{0.6}$Fe$_{0.4}$PO$_4$ cathode material. Rare Met. 2019; 38(1):29.

[17] Xu BL, Qi SH, Jin MM, Cai XY, Lai LF, Sun ZT, Han XG, Lin ZF, Shao H, Peng P, Xiang ZH, Elshof JET, Tan R, Liu C, Zhang ZX, Duan XC, Ma JM. 2020 roadmap on two-dimensional materials for energy storage and conversion. Chin Chem Lett. 2019;30(12):2053.

[18] Yang G, Jiang CY, He XM, Ying JR, Gao J. Preparation of Li$_3$V$_2$(PO$_4$)$_3$/LiFePO$_4$ composite cathode material for lithium ion batteries. Ionics. 2013;19:1247.

[19] Rui XH, Jin Y, Feng XY, Zhang LC, Chen CH. A comparative study on the low-temperature performance of LiFePO$_4$/C and Li$_3$V$_2$(PO$_4$)$_3$/C cathodes for lithium-ion batteries. J Power Sources. 2011;196(4):2109.

[20] Liu T, Wang B, Gu X, Wang L, Ling M, Liu G, Wang D, Zhang S. All-climate sodium ion batteries based on the NASICON electrode materials. Nano Energy. 2016;30:756.

[21] Jian Z, Zhao L, Pan H, Hu YS, Li H, Chen W, Chen L. Carbon coated Na$_3$V$_2$(PO$_4$)$_3$ as novel electrode material for sodium ion batteries. Electrochem Commun. 2013;14(1):86.

[22] Gaubicher J, Wurm C, Goward G, Masquelier C, Nazar L. Rhombohedral form of $Li_3V_2(PO_4)_3$ as a cathode in Li-ion batteries. Chem Mater. 2000;12:3240.

[23] Liu X, Li L, Li G. Partial surface phase transformation of Li_3VO_4 that enables superior rate performance and fast lithium-ion storage. Tungsten. 2019;1:276.

[24] Hongtong R, Thanwisai P, Yensano R, Nash J, Srilomsak S, Meethong N. Core-shell electrospun and doped $LiFePO_4$/FeS/C composite fibers for Li-ion batteries. J Alloys Compd. 2019;804:339.

[25] Wang Y, Alsmeyer DC, McCreery RL. Raman spectroscopy of carbon materials: structural basis of observed spectra. Chem Mater. 1990;2(5):557.

[26] Ren L, Li XE, Wang FF, Han Y. Spindle $LiFePO_4$ particles as cathode of lithium-ion batteries synthesized by solvothermal method with glucose as auxiliary reductant. Rare Met. 2015;34(10):731.

[27] Iermakova DI, Dugas R, Palacín MR, Ponrouch A. On the comparative stability of Li and Na metal anode interfaces in conventional alkyl carbonate electrolytes. J Electrochem Soc. 2015;162:A7060.

[28] Liao L, Zuo P, Ma Y, An Y, Yin G, Gao Y. Effects of fluoroethylene carbonate on low temperature performance of mesocarbon microbeads anode. Electrochim Acta. 2012;74:260.

[29] Gu XX, Xin LB, Li Y, Dong F, Fu M, Hou YL. Highly reversible Li–Se batteries with ultra-lightweight N, S-codoped graphene blocking layer. Nano Micro Lett. 2018;10:59.

[30] Tao Z, Xiao J, Wang H, Zhang F. Novel cathode structure based on spiral carbon nanotubes for lithium–sulfur batteries. J Electroanal Chem. 2019;851:113477.

[31] Sitinamaluwa HS, Li HN, Wasalathilake KC, Wolff A, Tesfamichael T, Zhang S, Yan C. Nanoporous SiO_x coated amorphous silicon anode material with robust mechanical behavior for high-performance rechargeable Li-ion batteries. Nano Mater Sci. 2019;1:70.

[32] Liu T, Zhao SX, Gou LL, Wu X, Nan CW. Electrochemical performance of Li-rich cathode material, $0.3Li_2MnO_3$–$0.7LiMn_{1/3}Ni_{1/3}Co_{1/3}O_2$ microspheres with F-doping. Rare Met. 2019;38(3):189.

[33] Gu XX, Yang Z, Qiao S, Shao CB, Ren XL, Yang JJ. Exploiting methylated amino resin as a multifunctional binder for high-performance lithium–sulfur batteries. Rare Met. 2020. https://doi.org/10.1007/s12598-020-01409-1.

[34] Wang B, Wang Q, Xu B, Liu T, Wang D, Zhao G. The synergy effect on Li storage of $LiFePO_4$ with activated carbon modifications. RSC Adv. 2013;3(43):20024.

[35] Gu XX, Lai C. One dimensional nanostructures contribute better Li–S and Li–Se batteries: progress, challenges and perspectives. Energy Stor Mater. 2019;23:190.